

A New Proposal to Jefferson Lab PAC48

Measurement of the Two-Photon Exchange Contribution to the Electron-Neutron Elastic Scattering Cross Section

S. Alsalmi (spokesperson)

King Saud University, Riyadh 11451, Saudi Arabia

E. Fuchey (spokesperson) and A.J.R. Puckett

University of Connecticut, Storrs, Connecticut 06269, USA

B. Wojtsekhowski (spokesperson), S. Barcus, A. Camsonne, J-P. Chen,

D. Gaskell, J.-O. Hansen, D. W. Higinbotham, M. Jones, C. Keppel, D. Mack,

D. Meekins, R. Michaels, B. Sawatzky, G. Smith, A. Tadepalli, and S. Wood

Thomas Jefferson National Accelerator Facility, Newport News, Virginia 23606, USA

K. Aniol

California State University, Los Angeles, CA 90032, USA

D. Armstrong, T. Averett, M. Satnik, Z. Wertz, and B. Yale

The College of William and Mary, Williamsburg, Virginia 23185, USA

J. Arrington and P. Reimer

Argonne National Laboratory, 9700 S Cass Ave, Lemont, Illinois 60439, USA

C. Ayerbe Gayoso, H. Bhatt, D. Bhetuwal, B. Devkota,

J. Dunne, D. Dutta, L. El-Fassi, and A. Karki

Mississippi State University, Mississippi State, MS 39762, USA

V. Bellini

Istituto Nazionale di Fisica Nucleare, I-95123 Catania, Italy

J. Bernauer

Stony Brook University, Stony Brook, NY 11794, US

Riken BNL Research Center, Upton, NY 11973, US

D. Biswas, M. E. Christy, B. Dongwi, I. P. Fernando, T. Gautam,
M. Kohl, A. Nadeeshani, J. Nazeer, T. Patel, and M. Rathnayake

Hampton University, Hampton, Virginia 23669, USA

W. Boeglin and P. Markowitz

Florida International University, Miami, FL 33199, USA

G. Cates, K. Gnanvo, N. Liyanage, and V. Nelyubin

University of Virginia, Charlottesville, Virginia 22904, USA

E. Cline

Stony Brook University, Stony Brook, NY 11794, US

E. Cisbani, F. Meddi, and G. Urciuoli

Istituto Nazionale di Fisica Nucleare - Sezione di Roma,

P.le Aldo Moro, 2 - 00185 Roma, Italy

J.C. Cornejo* and B. Quinn

Carnegie Mellon University, Pittsburgh, Pennsylvania 15213, USA

D. Hamilton and R. Montgomery

SUPA School of Physics and Astronomy,

University of Glasgow, Glasgow G12 8QQ, UK

F. Hauenstein

Old Dominion University, Norfolk, Virginia 23529, USA

T. J. Hobbs

Department of Physics, Southern Methodist University, Dallas, TX 75275, USA

Jefferson Lab, EIC Center, Newport News, VA 23606, USA

A. T. Katramatou and G.G. Petratos

Kent State University, Kent, OH 44242, USA

T. Kutz and A. Schmidt

The George Washington University, Washington, DC 20052, USA

D. Nguyen

Massachusetts Institute of Technology, Cambridge, MA 02139, USA

C. Petta and C. Sutera

Istituto Nazionale di Fisica Nucleare, Sezione di Catania, I-95123 Catania, Italy

A. Sarty

Saint Mary's University, Halifax, Nova Scotia B3H 3C3, Canada

K. Slifer

University of New Hampshire, Durham, NH 03824, USA

A. Shahinyan

AANL, 2 Alikhanian Brothers Street, 0036, Yerevan, Armenia

W. Tireman

Northern Michigan University, Marquette, Michigan 49855, USA

(Dated: December 5, 2020)

(* - TBC)

Abstract

We propose to make a high precision measurement of the two-photon exchange contribution (TPE) in elastic electron-neutron scattering at a four-momentum transfer $Q^2 = 4.5$ $(\text{GeV}/c)^2$. While significant efforts to study the two-photon-exchange have focused around elastic electron-proton scattering, the impact of TPE on neutron form factors was never examined experimentally. The proposed experiment will provide the very first assessment of the two-photon exchange in electron-neutron scattering, which will be important for understanding the nucleon form factor physics.

The proposed experiment will be performed in Hall A using the BigBite (BB) spectrometer to detect the scattered electrons and the Super-BigBite (SBS) to detect the protons and neutrons. The experiment should run concurrently with the E12-09-019 G_M^n and E12-17-004 G_E^n -Recoil experiments, which are expected to run in 2021. The experimental setup of the proposed experiment will be identical to that of E12-09-019 experiment.

The “ratio” method will be used to extract the electric form factor of the neutron G_E^n by scattering unpolarized electrons from deuterium quasi-elastically at two beam energies 4.4 and 6.6 GeV and electron scattering angles 41.9 and 23.3 degrees respectively. In the proposed approach, systematic errors are greatly reduced compared to those in the traditional single electron arm configuration. Several experiments at Mainz and JLab have used the ratio method to measure the neutron magnetic form factor in the past years. The method can be extended to extract the neutron electric form factor even with less stringent requirements on the knowledge of the absolute neutron detection efficiency and experimental kinematics than required for neutron magnetic form factor measurements.

I. INTRODUCTION

In 1950s, a series of experiments performed by R. Hofstadter [1] revealed that nucleons have a substructure (which corresponds to our modern view in terms of quarks and gluons). The experiment confirmed M. Rosenbluth's theory of electron scattering [2] based on the one-photon exchange approximation. In this so-called Born approximation, where the interaction between the electron and the nucleon occurs *via* an exchange of one virtual photon (OPE), the unpolarized $e - N$ elastic cross section can be parameterized in terms of a nucleon magnetic, G_M , and electric, G_E , form factors. These form factors describe the deviation from a point-like scattering cross section, σ_{Mott} :

$$\left(\frac{d\sigma}{d\Omega} \right)_{eN \rightarrow eN} = \frac{\sigma_{Mott}}{\epsilon(1 + \tau)} [\tau \cdot G_M^2(Q^2) + \epsilon \cdot G_E^2(Q^2)], \quad (1)$$

where E and E' are the incident and scattered electron energies, respectively, θ is the electron scattering angle, $\tau \equiv -q^2/4M^2$, with $-q^2 \equiv Q^2 = 4EE' \sin(\theta/2)$ being the negative four momentum transfer squared, M is the nucleon mass, and $\epsilon = [1 + 2(1 + \tau) \tan^2(\theta/2)]^{-1}$ is the longitudinal polarization of the virtual photon. The reduced cross section is defined by:

$$\sigma_r \equiv \left(\frac{d\sigma}{d\Omega} \right) \cdot \frac{\epsilon(1 + \tau)}{\sigma_{Mott}} = \tau \cdot G_M^2(Q^2) + \epsilon \cdot G_E^2(Q^2) = \sigma_T + \epsilon \cdot \sigma_L, \quad (2)$$

where σ_L and σ_T are the cross sections for longitudinally and transversely polarized virtual photons, respectively.

The linear ϵ dependence of the cross section is due to the σ_L term. The ratio σ_L/σ_T is the so-called Rosenbluth slope related to G_E/G_M (in OPE), see Fig. 1. The data show that at Q^2 of 4-5 (GeV/c)² the Rosenbluth slope is three to four times larger than expected in OPE (shown as the dot-dashed line in Fig. 1) for the observed values of the G_E^p/G_M^p ratio.

The nucleon electromagnetic form factors can reveal a lot of information about the nucleon internal structure, as well as the quark distribution. The form factors depend only on one variable, the negative square of the four-momentum transfer carried by the photon, Q^2 . In

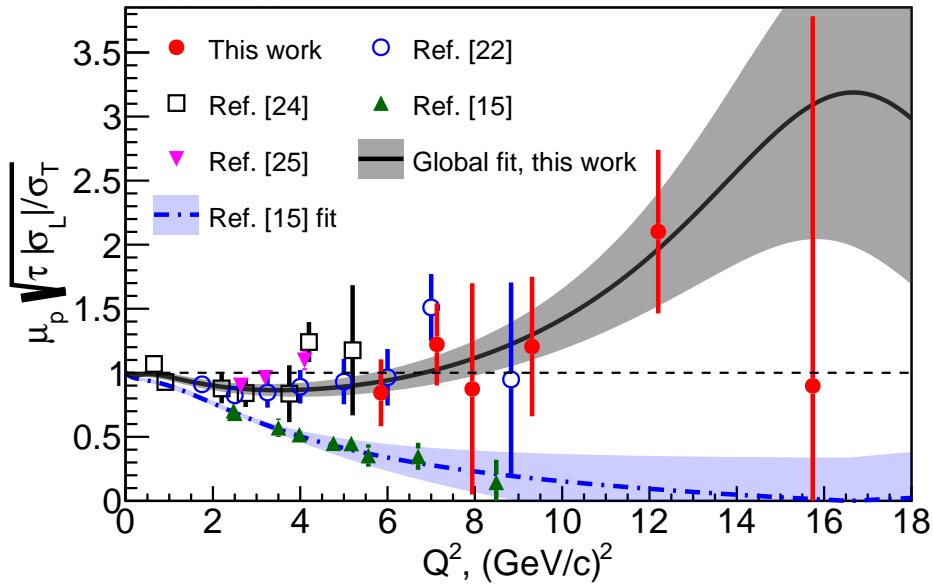


FIG. 1. The square root of Rosenbluth slope, corrected for kinematical factor $\sqrt{\tau}$ and μ_p , observed in elastic electron-proton scattering, adopted from Ref. [3]. References in the plot are also from Ref. [3]

the limit of large Q^2 , perturbative QCD (pQCD) provides well-motivated predictions for the Q^2 -dependence of the form factors and their ratio. However, it was never predicted at what Q^2 range the pQCD prediction (scaling) will be valid. Studies show that pQCD validity will require a very large Q^2 of 100 (GeV/c)^2 . It was discovered at JLab, using the double polarization methods, that the proton electric and magnetic form factors behave differently starting at $Q^2 \approx 1 \text{ (GeV/c)}^2$.

Experimentally, the nucleon form factors can be measured using one of two techniques: the polarization transfer technique and the Rosenbluth technique. The polarization method examines the polarization transfer from longitudinally polarized electron to the recoiling nucleon and determine the resulting azimuthal asymmetry distribution using a polarimeter. Alternatively, one can use a polarized electron beam and polarized target. In the Rosenbluth method, the electric and magnetic form factors can be separated by making two or more measurements with different ϵ values (*i.e.* different beam energies and angles), but with same Q^2 value. The Rosenbluth technique requires an accurate measurement of the cross section

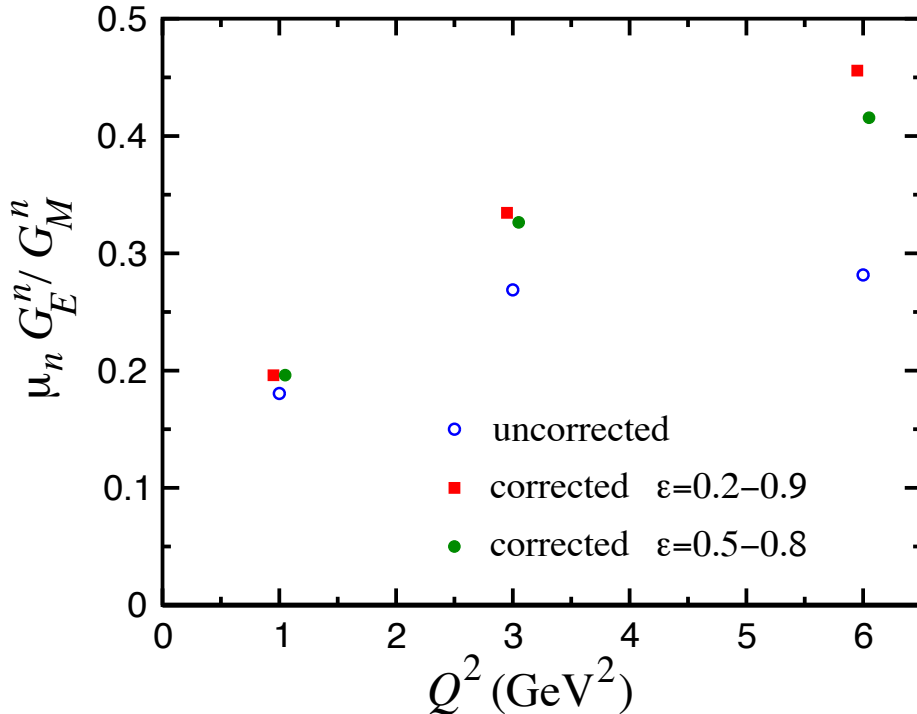


FIG. 2. Projected impact of TPE on G_E^n/G_M^n using LT separation, according to Ref. [4].

and suffers from large systematic uncertainties arising from several factors, for instance the need for a precise determination of the scattering angle. Additionally, for a measurement of the neutron form factors, accurate knowledge of the neutron detector efficiency is required, which is particularly hard to achieve. These uncertainties can be greatly reduced by measuring the ratio of $e - n$ and $e - p$ quasi-elastic cross sections.

When comparing the values of G_E^n/G_M^n obtained from both techniques, a significant discrepancy was observed (see Fig. 1). Such a discrepancy implies a potential problem in our understanding of the nucleon substructure. Many efforts were made to explain this effect, and it is believed that the inconsistency is due to the contribution of two-photon exchange in $e - N$ elastic scattering process [5, 6]. Predictions made for the neutron case are shown in Fig. 2 , adopted from [4]. The contribution of TPE could reach about 30% of the Rosenbluth slope value at 5 (GeV/c) 2 .

50 In the following we propose to make a precision L/T separation of the elastic electron-
51 neutron cross section and first experimental assessment of the two-photon exchange contribu-
52 tion on the neutron magnetic form factor measurements (see also Ref. [7]). The result of
53 the nTPE experiment will likely add a new component to our understanding of the elastic
54 electron-nucleon process.

55

II. PHYSICS MOTIVATION

56 The nucleon plays the same central role in hadronic physics that the hydrogen atom does
 57 in atomic physics and the deuteron in the physics of nuclei. The structure of the nucleon
 58 and its specific properties, such as charge, magnetic moment, size, mass; the elastic electron
 59 scattering form factors, resonances; and structure functions in DIS, are of fundamental sci-
 60 entific interest. The isospin is a fundamental property of the nucleon, so both the proton
 61 and neutron investigations are important to do. By using data on the proton and neutron
 62 form factors the flavour structure could be explored [8]. It has already provided the most
 63 direct evidence for a diquark correlation in the nucleon [9–11].

64 Hadron structure, as seen in elastic electron scattering, in one-photon approximation, is
 65 defined by two functions of four momentum transfer square. They are: the helicity con-
 66 serving Dirac form factor, F_1 , which describes the distribution of the electric charge, and
 67 the helicity non-conserving Pauli form factor, F_2 , which describes the distribution of the
 68 magnetic moment. These two form factors are the ingredients of the hadronic current. They
 69 contain information on the transverse charge distribution for an unpolarized and transversely
 70 polarized nucleon, respectively, in the infinite momentum frame [12, 13].

71 The Sachs form factors, G_E and G_M , the ratio of which will be extracted directly from
 72 the data, are related to F_1 and F_2 by

$$F_1 = \frac{G_E + \tau G_M}{1 + \tau} \quad \text{and} \quad F_2 = \frac{G_M - G_E}{\kappa(1 + \tau)}, \quad (3)$$

73 where κ is the nucleon anomalous magnetic moment.

74 Already twenty-four years ago, an important development in QCD phenomenology has
 75 been the exploration of the generalized parton distribution (GPD) formalism [14–16], which
 76 provides relations between inclusive and exclusive observables. The nucleon elastic form
 77 factors F_1 and F_2 are given by the first moments of the GPDs

$$F_1(t) = \sum_q \int_0^1 H^q(x, \xi, t, \mu) dx \quad \text{and} \quad F_2(t) = \sum_q \int_0^1 E^q(x, \xi, t, \mu) dx, \quad (4)$$

78 where H^q and E^q are two of the generalized parton distributions, x is the standard Bjorken
 79 x , ξ is the “skewness” of the reaction, t is the four-momentum transferred by the electron,

μ is a scale parameter necessary for the evolution over Q^2 , analogous to DIS parton distributions, and the sum is over all quarks and anti-quarks. GPDs may be accessed through processes such as deeply virtual Compton scattering, where the interaction is factorized into a hard part with the virtual photon/photon interactions with an individual quark and a soft part of the residual system where the GPD information is contained.

A fundamental nucleon feature, the spin, is related to GPDs, as shown by X. Ji [15]. The moments of GPDs can yield information, according to Ji's Angular Momentum Sum Rule, on the contribution to the nucleon spin from quarks and gluons, including both the quark spin and orbital angular momentum.

At present, experimental measurements of GPDs are still scarce. Until high Q^2 DVCS data becomes available, work has been done to attempt to parameterize these GPDs, which rely heavily on data from electromagnetic form factors and parton distributions from DIS as constraints [17]. Data at high Q^2 for G_E^n would contribute significantly in the development of these models.

As we presented above, nucleon elastic form factors provide important input for the modeling of GPDs. At the same time, the measured cross section of elastic $e - p$ scattering at high Q^2 is significantly larger than predicted by Born-approximation calculations [18], indicating that TPE effects play a critical role in the high- Q^2 region and therefore must be well understood before conclusions about GPDs can be drawn.

99

III. TECHNIQUE

100 This proposal is based on instrumentation, simulation, and analysis development made
 101 by the GMn/SBS collaboration for the GMn, E12-09-019, experiment [19]. The GMn experi-
 102 ment is one of several form factor experiments approved by JLab PAC. The SBS spectrometer
 103 was funded by DOE with large contributions provided by the collaborating institutions from
 104 USA, Italy, UK, and Canada. The apparatus and DAQ installation will start in 2020 and
 105 the data taking run is expected to be in summer-fall 2021.

106 The neutron form factors are challenging to be determine experimentally especially be-
 107 cause there is no free neutron target. However, since deuterium is a loosely coupled system,
 108 it can be viewed as the sum of a proton target and a neutron target. In fact, quasi-elastic
 109 scattering from deuterium has been used to extract the neutron magnetic form factor, G_M^n ,
 110 at modestly high Q^2 for decades [20, 21] in the single arm (e, e') experiments. However, the
 111 proton cross section needs to be subtracted by applying a single-arm quasi-elastic electron-
 112 proton scattering. This “proton-subtraction” technique suffers from a number of systematic
 113 uncertainties e.g. contributions from inelastic and secondary scattering processes.

114 Many years ago, L. Durand [22] proposed the so-called “ratio-method” based on the
 115 measurement of both $D(e, e'n)$ and $D(e, e'p)$ reactions. In this method, many of the system-
 116atic errors are canceled out. Several experiments [23–25] have applied the ratio-method to
 117 determine the neutron magnetic form factor.

118 The GMn/SBS experiment [19] will take data for elastic $e - n$ scattering for several
 119 kinematics with Q^2 from 3.5 up to 13.5 $(\text{GeV}/c)^2$. We propose to use this method to measure
 120 the Rosenbluth slope and extract (in OPE approximation) the neutron electric form factor,
 121 G_E^n , at one value of momentum transfer. In fact, one of the required data points will be taken
 122 by the GMn experiment, so an additional measurement is needed only for one kinematics.

123 Data will be collected for quasi-elastic electron scattering from deuterium in the process
 124 $D(e, e'n)p$. Complementary $D(e, e'p)n$ data will be taken to calibrate the experiment appa-
 125 ratus. The current knowledge of the $e - p$ elastic scattering cross section (obtained in the
 126 single arm $H(e, e')p$ and $H(e, p)e'$ experiments) will be also used for precision determination
 127 the experiment kinematics.

128 Applying the Rosenbluth technique to measure G_E^n requires accurate measurement of the
 129 cross section and suffers from large uncertainties. To overcome this issue, we propose to
 130 extract the value of G_E^n from the ratio of quasi-elastic yields, $R_{n/p}$, in scattering from a
 131 deuteron target as follows:

$$R_{n/p} \equiv R_{observed} = \frac{N_{e,e'n}}{N_{e,e'p}} \quad (5)$$

132 $R_{observed}$ needs to be corrected to extract the ratio of e-n/e-p scattering from nucleons:

$$R_{corrected} = f_{corr} \times R_{observed}, \quad (6)$$

133 where the correction factor f_{corr} takes into account the variation in the hadron efficiencies
 134 due to changes of the $e - N$ Jacobian, the radiative corrections, and absorption in path from
 135 the target to the detector, and small re-scattering correction.

136 In one-photon approximation, $R_{corrected}$ can be presented as:

$$R_{corrected} = \frac{\sigma_{Mott}^n \cdot (1 + \tau_p)}{\sigma_{Mott}^p \cdot (1 + \tau_n)} \times \frac{\epsilon \sigma_L^n + \sigma_T^n}{\epsilon \sigma_L^p + \sigma_T^p} \quad (7)$$

It is important that the ratio $R_{Mott} = \frac{\sigma_{Mott}^n \cdot (1 + \tau_p)}{\sigma_{Mott}^p \cdot (1 + \tau_n)}$ could be determined with very high relative accuracy even with modest precision for the beam energy, electron scattering angle, and detector solid angle. Now, let us write the $R_{corrected}$ at two values of ϵ using $S^{n(p)} = \sigma_L^{n(p)} / \sigma_T^{n(p)}$ as:

$$R_{corrected,\epsilon_1} = \frac{\epsilon_1 \sigma_L^n + \sigma_T^n}{\epsilon_1 \sigma_L^p + \sigma_T^p} \quad R_{corrected,\epsilon_2} = \frac{\epsilon_2 \sigma_L^n + \sigma_T^n}{\epsilon_2 \sigma_L^p + \sigma_T^p}$$

In these two equations there are two unknown variables: σ_L^n and σ_T^n . We remind here that proton and neutron measurements are made simultaneously with the same apparatus. Thanks to this, the dominant contribution to the uncertainty of the Rosenbluth slope of the reduced cross section vs. ϵ , $S^n = \sigma_L^n / \sigma_T^n$, will come from the uncertainty of S^p . At $Q^2=4.5$ (GeV/c)², according to the global analysis of $e - p$ cross section [3], the value of S^p is close to $1/(\tau \mu_p^2) = 0.087$ with an uncertainty of 0.01. The resulting equation for S^n is:

$$A = B \times \frac{1 + \epsilon_1 S^n}{1 + \epsilon_2 S^n} \approx B \times (1 + \Delta \epsilon \cdot S^n),$$

¹³⁷ with $\Delta\epsilon = \epsilon_1 - \epsilon_2$, and where the variable $A = R_{corrected,\epsilon_1}/R_{corrected,\epsilon_2}$ will be measured
¹³⁸ with statistical precision of 0.1%. Assuming, for this estimate, equal values of Q^2 for two
¹³⁹ kinematics, the τ and σ_T for two kinematics are canceled out, and the variable

$$B = (1 + \epsilon_2 S^p)/(1 + \epsilon_1 S^p) \quad (8)$$

¹⁴⁰ For actual small range of ϵ and small value of the slope, $B \approx (1 - \Delta\epsilon \cdot S^p)$. The value of
¹⁴¹ B will be determined from global proton $e - p$ data to a precision of 0.25×0.01 .

¹⁴² At $Q^2=4.5$ (GeV/c)² the ratio $\mu_n G_E^n/G_M^n$ is 0.55 ± 0.05 based on polarization transfer data
¹⁴³ which is mostly insensitive to the two-photon exchange, see the 2015 review from Perdrisat
¹⁴⁴ *et al.* [26]. In the simplest model, the slope S^n is a sum of the slope due to G_E^n/G_M^n and the
¹⁴⁵ neutron two-photon exchange nTPE contribution:

$$S^n = (G_E^n/G_M^n)^2/\tau + \text{nTPE} \quad (9)$$

¹⁴⁶ Without the nTPE contribution, our projected measured slope would be $S^n = (G_E^n/G_M^n)^2/\tau =$
¹⁴⁷ 0.063 .

¹⁴⁸ If we use the prediction available in [4] which is reproduced on our Fig. 2, nTPE leads
¹⁴⁹ to increase of the neutron Rosenbluth slope S^n by a factor 2; Under this assumption, the
¹⁵⁰ projected measured Rosenbluth slope would now become $S^n = 0.126$, and nTPE would then
¹⁵¹ be:

$$\text{nTPE} = S^n - (G_E^n/G_M^n)^2/\tau = 0.063. \quad (10)$$

¹⁵² The projected measurement of the neutron two-photon exchange for this experiment is
¹⁵³ $nTPE = 0.063 \pm 0.012 \pm 0.01$, where the first uncertainty is due to accuracy of G_E^n/G_M^n and
¹⁵⁴ the second one due to projected precision of this experiment. It would be a 4-4.5 sigma
¹⁵⁵ observation of the two-photon exchange contribution for the neutron.

156

IV. PROPOSED MEASUREMENTS

157 We propose to use the same experimental setup of the E12-09-019 experiment. We will
 158 add a kinematic point at $Q^2 = 4.5 \text{ (GeV/c)}^2$, at a higher beam pass (6.6 GeV/3 pass instead
 159 of 4.4 GeV/2 pass), leading to a higher ϵ value. This additional point along with the data
 160 point of the E12-09-019 experiment will allow us to perform the standard Rosenbluth method
 161 to obtain (in one-photon approximation) the neutron electric and magnetic form factors. In
 162 addition, the ratio method (Sec. III), in which the systematic errors are greatly reduced, will
 163 be implemented to calculate the two photon exchange (TPE) contribution. The study of
 164 the ϵ dependence of the reduced cross section will help examine the two photon exchange
 165 contribution to the neutron form factor ratio G_E^n/G_M^n . Table. I displays the kinematic settings
 166 of the proposed experiment.

Point	Q^2 $(\text{GeV}/c)^2$	E (GeV)	E' (GeV)	θ_{BB} degrees	θ_{SBS} degrees	ϵ
1	4.5	4.4	2.0	41.88	24.67	0.599
2	4.5	6.6	4.2	23.23	31.2	0.838

TABLE I. Kinematic settings of the proposed experiment. The kinematic point with the lowest ϵ value (blue row) is an existing measurement of the approved E12-09-019 experiment.

167

V. EXPERIMENTAL SETUP

168 As illustrated in Fig. 3, this experiment will study electron scattering from a 15 cm long
 169 liquid Deuterium target held in a vacuum. The scattered electron will be detected in the
 170 BigBite spectrometer with an upgraded electron detector stack. The neutron arm is arranged
 171 with a dipole magnet 48D48 (SBS) and a segmented hadron calorimeter HCAL. The whole
 172 detector package was designed and is being assembled for the GMn, E12-09-019, experiment.

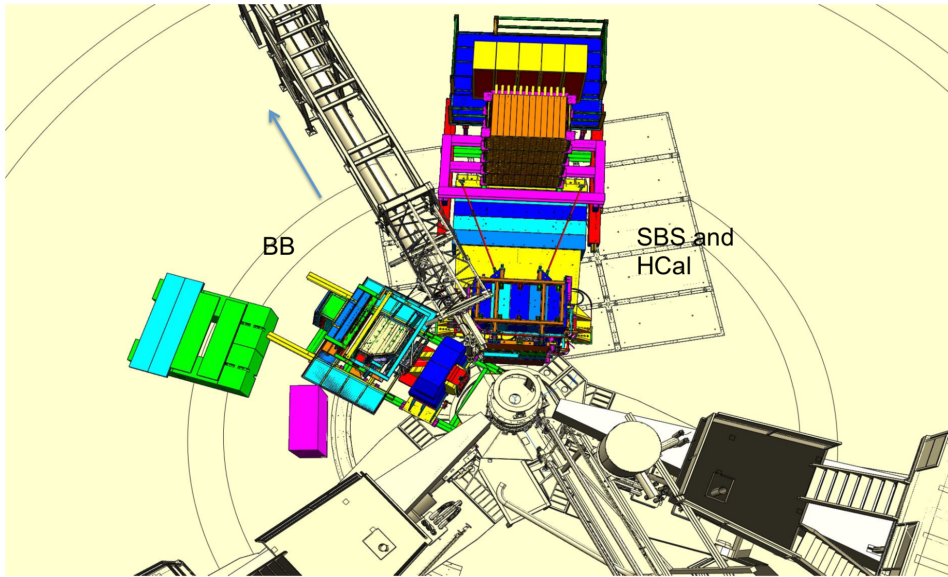


FIG. 3. Layout of the experimental setup in nTPE.

173

1. Parameters of the SBS

174 The 48D48 magnet from Brookhaven was acquired as part of the Super Bigbite project
 175 and will be available for this experiment. It consists of a large dipole magnet which provides
 176 a field integral of about $1.7 \text{ T} \cdot \text{m}$, allowing for quasielastic protons to be sufficiently deflected
 177 to allow clear differentiation from neutrons. The active field volume has an opening of $46 \times$
 178 $25 \text{ vertical} \times \text{horizontal}$), matching the aspect ratio of the neutron arm, and a depth of 48
 179 cm.

180 The placement of this magnet will be 1.6 m away from the target, which would normally

¹⁸¹ interfere with the beamline. To accommodate this, modifications were made to the iron yoke
¹⁸² such that the beamline will pass through the magnet yoke area.

¹⁸³ The field configuration will be such that positively charged particles will be deflected
¹⁸⁴ upwards away from the hall floor. For a field integral of 1.7 Tesla-m, protons of momentum
¹⁸⁵ 2.5 GeV/c will be deflected 250 mrad, which translates to a displacement of 1.29 m. Including
¹⁸⁶ expected detector resolution, the $p_{miss,\perp}$ distribution will be similar to what was seen in
¹⁸⁷ E02-013, so cuts of < 100 MeV/c will be appropriate. Monte Carlo simulations show a
¹⁸⁸ contamination of charged quasielastics to be negligible.

¹⁸⁹ The presence of the magnet also works to sweep low energy charged particles from the
¹⁹⁰ target away from the neutron arm. Particles of momentum less than 1.3 GeV/c will be
¹⁹¹ entirely swept outside of the neutron arm acceptance. This greatly reduces the amount of
¹⁹² charged low energy background.

193

A. The BigBite Spectrometer

194 Scattered electrons will be detected in the BigBite spectrometer. The spectrometer con-
 195 sists of a single dipole magnet (with magnetic field approximately 1.2 T) and a detection
 196 system, see Fig. 4.

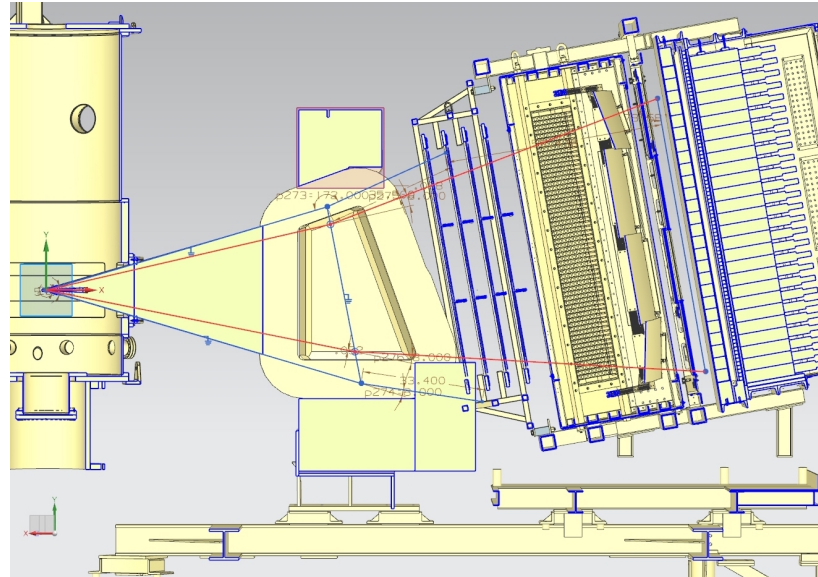


FIG. 4. The BigBite spectrometer with the upgraded detector stack.

197

1. GEM Chambers

198 To perform the tracking of charged particles under the high rates anticipated for this
 199 experiment, the drift chambers were replaced with gas electron multiplier (GEM) detectors.
 200 These detectors have proven to be capable of operating under luminosities of 25 kHz/mm^2
 201 for the COMPASS experiment at CERN and the spatial resolution of each of these chambers
 202 is anticipated to be about $70 \mu\text{m}$. There will be two sets of GEMs placed on each side of the
 203 GRINCH Cherenkov detector.

204 The set of GEMs in front of the GRINCH is composed of four layers of GEMs. Two of
 205 these layers have been built by the SBS collaborators from INFN. They are composed three

206 modules each, measuring $40 \times 50 \text{ cm}^2$, such that each layer covers $40 \times 150 \text{ cm}^2$ (the
 207 long dimension being vertical, along the dispersive direction). The readout of these modules
 208 are oriented in the x/y direction *i.e.* parallel and perpendicular to the dispersive direction
 209 (horizontal and vertical). The two other layers are being built by the SBS collaborators from
 210 UVA. They are composed of a single module measuring $40 \times 150 \text{ cm}^2$, the long dimension
 211 again being vertical and along the dispersive direction. The readout of these modules are
 212 oriented in the u/v direction *i.e.* ± 30 degrees with respect to the horizontal direction.

213 The set of GEMs behind the GRINCH has been built by the SBS collaborators from
 214 UVA. It is composed of a single layer composed of four modules measuring $50 \times 60 \text{ cm}^2$,
 215 such that the layer covers $60 \times 200 \text{ cm}^2$ (the long dimension again being along the dispersive
 216 direction). The readout of these modules are all oriented in the x/y direction.

217 The background levels in the GEMs have been evaluated, with the help of the G4SBS
 218 simulation package([27] and Sec. VI) for the G_M^n experimental readiness review. For the
 219 G_M^n highest Q^2 point (which is the most constraining, since it combines mandatory maxi-
 220 mum luminosity and smaller BigBite angles), the rates in the front GEMs are of the order
 221 of 120 kHz/cm^2 for the front GEM layers, and below 50 kHz/cm^2 for the back GEM. To
 222 perform the GEM tracking within such a high-rate environment, we use the cluster recon-
 223 structed in the BigBite shower as a track seed to clean the large combinatorics that would
 224 otherwise be created by the large number of hits. After this, the main challenge is the
 225 separation by the clustering algorithm of the signal and background hits to minimize track
 226 smearing. At this level of background, a TreeSearch tracking algorithm combined with a
 227 fairly simple cluster separation algorithm has already proven to achieve 70% efficiency at
 228 nominal luminosity. A better cluster separation algorithm is currently being developed and
 229 should allow to significantly improve this figure.

230

2. Shower/Preshower

231 The electromagnetic calorimeter configuration consists of two planes of lead glass blocks
 232 which we call the preshower and shower. The preshower, located about 80 cm behind the
 233 first GEM chamber, consists of a 2×26 plane of $37 \text{ cm} \times 9 \text{ cm}$ blocks. The shower, about

²³⁴ 1 m behind the first GEM chamber, consists of an 7×27 array of 8.5 cm \times 8.5 cm blocks.
²³⁵ Sums over these blocks form the physics event trigger for the experiment.

²³⁶ The preshower signal can be used to provide an additional method of pion rejection.
²³⁷ By selecting low preshower signals, a pion rejection factor of 1:50 can be achieved through
²³⁸ optimization. Despite higher particle rates, pion rejection performance is anticipated to
²³⁹ be similar to that achieved for Transversity, E06-010. By measuring the pedestal widths
²⁴⁰ and resolution for E06-010 and scaling to this proposal’s conditions, overall relative energy
²⁴¹ resolution for the detector is expected to become worse by a factor of 1.6, to about $\sigma_{\delta E/E} =$
²⁴² 25%.

²⁴³ *3. Timing hodoscope*

²⁴⁴ The BigBite timing hodoscope has been built by the SBS collaborators from Glasgow to
²⁴⁵ replace the BigBite scintillator plane. It will be composed of 90 bars stacked in a plane,
²⁴⁶ each with dimensions 1 in. \times 1 in. \times 60 cm. The paddle stack will be oriented such that
²⁴⁷ the long dimension of the bars is horizontal *i.e.* perpendicular to the dispersive direction.
²⁴⁸ Each of these elements are read out by a PMT on each side, mostly to provide measurement
²⁴⁹ redundancy.

²⁵⁰ This plane will primarily be used to provide a signal for nucleon time of flight reconstruc-
²⁵¹ tion. A time resolution of 200 ps is anticipated. This fine segmentation is meant to lower the
²⁵² rates in the detector. Background studies made for the G_M^n experimental readiness review
²⁵³ demonstrated that the rates experienced by each element was \leq 500 kHz at a luminosity of
²⁵⁴ 2.8×10^{38} cm $^{-2}$ s $^{-2}$. Signals from the PMTs are processed by NINO front-end cards which,
²⁵⁵ when the PMT pulse crosses the NINO threshold, will produce a digital signal to be read
²⁵⁶ out by CAEN 1190 TDCs which record a leading time and a trailing time.

²⁵⁷ *4. GRINCH cherenkov detector*

²⁵⁸ The main purpose of the GRINCH is to provide additional particle identification for offline
²⁵⁹ pion rejection. The GRINCH consists of a tank with a maximum depth of 88.9 cm, with 4

260 cylindrical mirrors focusing the cherenkov light directly onto a 510 PMT array (60 lines of
261 PMTs, with lines of 9 PMTs alternating with lines of 8 PMTs) placed away from the beam.
262 The radiation gas will be C_4F_8 , which is by far the best compromise between light yield
263 for electrons and operating cost. With $n - 1 = 1.35 \times 10^{-3}$, the π threshold is only about
264 2.7 GeV, so the additional pion rejection will be most effective below this threshold.

265 Similar to the timing hodoscope, the signals from the GRINCH PMTs pulses are processed
266 by NINO front-end cards which, when the PMT pulse crosses the NINO threshold, will
267 produce a digital signal to be readout by VETROC TDCs, which for each PMT hit will
268 record a leading time and a trailing time. The analog signal will not be recorded however,
269 which means that for each PMT hit, the information of the number of photoelectrons is not
270 directly available (although it can in theory be deduced from the time over threshold).

271 All of this implies that the electron selection relies on the number of GRINCH PMT
272 firing, instead of relying on the signal amplitude.

273

B. Hadron Calorimeter (HCal)

274

1. Description

275 The Hadron Calorimeter (HCal) has been designed specifically to measure the recoil
 276 nucleon for the SBS experiments. Specifically for this experiment (and for G_M^n), HCal
 277 combined with the SBS (48D48) magnet provides identification of the recoil nucleon, as
 278 well as additional kinematic constraint and possibly timing information on the measured
 279 interaction. Nucleon identification is illustrated on Fig. 5. This figure shows the compared
 280 proton and neutron position distribution in HCal at the same electron kinematics. The
 281 proton distribution is being shifted upwards by about 1 m compared to the neutron.

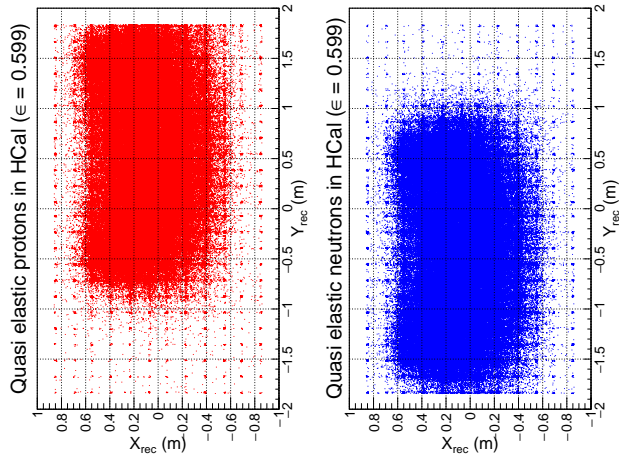


FIG. 5. Reconstructed HCal cluster from quasi-elastic events generated by G4SBS. The left distribution in red is for the proton, the right distribution in blue is for the neutron.

282

The HCal (a CAD model of which is shown in Fig. 6) is composed of 288 modules arranged
 283 in an array of 12×24 . In front of the full assembly is located a $3/4$ – inch steel plate which
 285 serves two purposes:

286

- initiate the hadronic shower to optimize the calorimeter response;
- shield the modules from a fraction of the low energy secondaries;

287

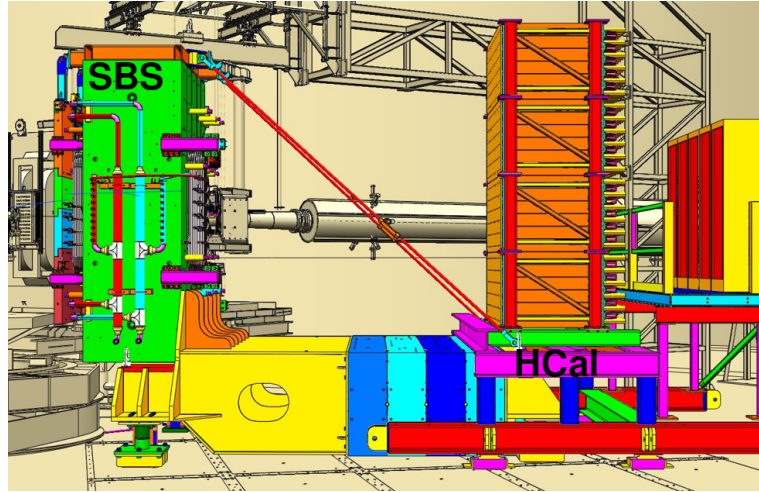


FIG. 6. CAD representation of HCal (right) with the SBS magnet (left)

288 Each of these modules measures $6 \times 6 \text{ in}^2$ section, for 3 ft length. They are composed of
 289 alternating tiles of scintillators and iron around a central light guide which collects the light
 290 generated in the scintillators by the hadronic shower, and guides it to the PMT at the end of
 291 the block. Cosmic tests have determined that the average light yield for the HCal modules
 292 is around 5 photoelectrons per MeV deposited in the scintillator tiles.

293 The PMTs are read out with FADC250 which sample the PMT signal every 4 ns and
 294 allow to reconstruct the PMT pulse shape, and hence its timing. They are also read out by
 295 TDCs which provide additional timing information. Thanks to this, the timing resolution
 296 can be better than 1 ns, which cosmic tests (in progress) seem to confirm.

297 The energy resolution is intrinsically broad (see Fig. 11 in Section VI), due mostly to the
 298 small fraction of energy from the hadronic shower actually measured by the scintillator tiles
 299 (≤ 0.1 - refer yet again to Fig. 11).

300

2. Discussion on HCal efficiency

301 A crucial parameter of this experiment is the hadron calorimeter efficiency, which is
 302 expected to be slightly different for protons and neutrons, and more importantly the efficiency
 303 stability.

304 The calorimeter efficiency will be measured by using "elastic" reactions $H(e, e)p$, $H(\gamma, \pi^+)n$
 305 and more with $D(\gamma, \pi^+)n$ and $D(\gamma, \pi^-)p$ single pion production. Fig. 7 (a) shows the pro-
 306 jected proton position from $H(e, e)p$, Fig. 7 (b) shows the projected proton position from
 307 $H(\gamma, \pi^+)n$. In each case, the trigger will not use the nucleon detector information. Analysis

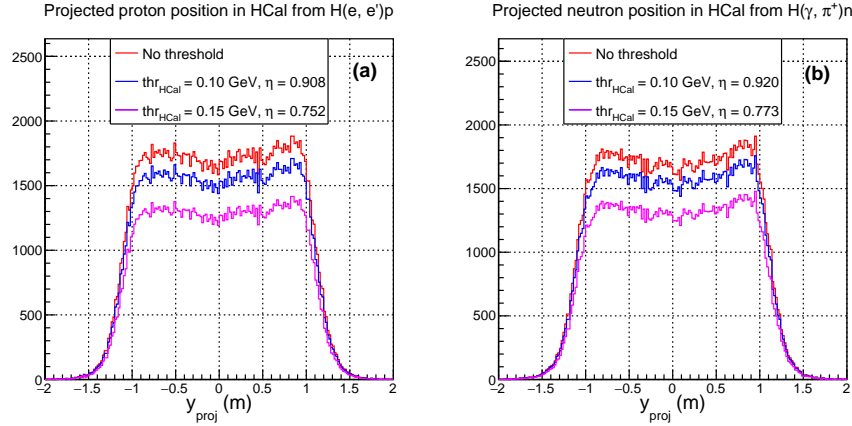


FIG. 7. Projected position in HCal in for the protons in $H(e, e)p$ (a) and the neutrons in $H(\gamma, \pi^+)n$ (b). On both panels, red distributions show the projected distribution for p, n , not detected; blue distributions show the distribution for p, n detected with a 0.1 GeV threshold; magenta distributions show the distribution for p, n detected with a 0.15 GeV threshold.

308
 309
 310 will use the amplitude distribution in the same way as done on Fig. ?? with the red dis-
 311 tributions. Blue distributions on Fig. 7 show the expected Y distribution applying a 0.10
 312 GeV threshold on HCal; Magenta distributions on Fig. 7 show the expected Y distribution
 313 applying a 0.15 GeV threshold on HCal. As reported in the E12-09-019 GMn proposal[?]
 314 on Table 8, the expected recorded statistics for $H(\gamma, \pi^+)n$ are of the order of 4000 events,
 315 which will represent a relative 1.5% uncertainty on the neutron efficiency. The recorded
 316 statistics for $H(e, e)p$ are of the order of 82000 events, which will represent a relative 0.3%
 317 uncertainty on the proton efficiency.

318
 319 The specific value of the hadron calorimeter efficiency does not impact the quality of the
 320 experimental result. However, the stability of the efficiency ratio is essential.

321 Let us evaluate in detail the influence of the hadron efficiencies, η_n and η_p , on the exper-

imental result. The S^n result is sensitive only to the ratio of neutron efficiency to proton efficiency, $R_\eta = \eta_n/\eta_p$. Such a ratio is very stable because the nucleon momenta are the same by definition of the Rosenbluth method. We have a plan to monitor the stability of this ratio in our experimental data.

Our primary experimental observable is the ratio of yields $R_{n/p} = N_{en}/N_{ep}$. In this experiment, the parameter of interest is $A = [R_{n/p,\epsilon-1}/R_{n/p,\epsilon-2}] \times [R_{\eta,epsilon-1}/R_{\eta,epsilon-2}]$.

As we wrote in our proposal, pages 12 and 13, and under the assumption that the reduced cross section σ_R is linear in ϵ , the neutron Rosenbluth slope S^n can be obtained as:

$$S^n = \frac{A - 1}{\Delta\epsilon} + S^p = \left(\frac{R_{n/p,\epsilon-1}}{R_{n/p,\epsilon-2}} \times \frac{R_{\eta,epsilon-1}}{R_{\eta,epsilon-2}} - 1 \right) / \Delta\epsilon + S^p \quad (11)$$

As it is easy to see from the formula above, the efficiency impact cancels out in S^n if the efficiency ratio is stable.

The procedure to evaluate the hadron detector efficiency was presented on the Monday write-up (see below). The result will be fitted by a few parameter functions, and the ratio of efficiency R_η is characterized by those parameters as well as the threshold. This study will be performed for all modules of HCal used in the experiment. After the data collection, we will repeat this study with the recorded data for each kinematic. Based on projected statistics of a few million events, the accuracy of R_η will be better than 0.1%. With such an accuracy, we will monitor the stability of R_η . This corresponds to the uncertainty in S^n , using the formula above, of 0.004, with our $\Delta\epsilon = 0.24$.

Additional analysis of the efficiency ratio is presented on Fig ???. This analysis focused on absolute value of efficiency ratio, for which we expect 1% statistical level. To monitor the stability, we will have hundreds of times more statistics.

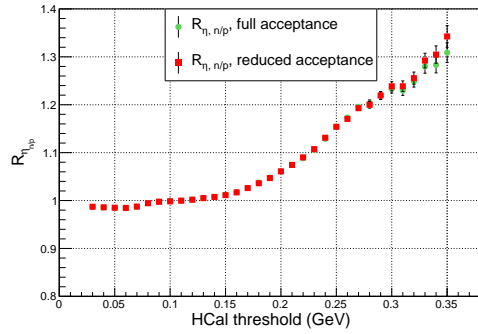


FIG. 8. Neutron/proton efficiency ratio $R_{\eta_n/p}$ as a function of the calorimeter threshold, for our quasi-elastic sample. The error bars represent the uncertainty from the calibration measurements discussed earlier. The green represents $R_{\eta_n/p}$ on the full acceptance, the red represents $R_{\eta_n/p}$ on a reduced acceptance.

344 **VI. SIMULATIONS, ESTIMATIONS OF COUNTING RATES AND**
 345 **ACCIDENTALS**

346 The estimates of counting rates accidentals have been performed using G4SBS, the
 347 GEANT4-based simulation package developed for the SBS experiment [27]. This package
 348 includes a wide range of event generators, which allows us to evaluate the rates for both
 349 events of interest (signal) and background. The representation of the experiment apparatus
 350 in G4SBS is shown in the high ϵ configuration in Fig. 9.

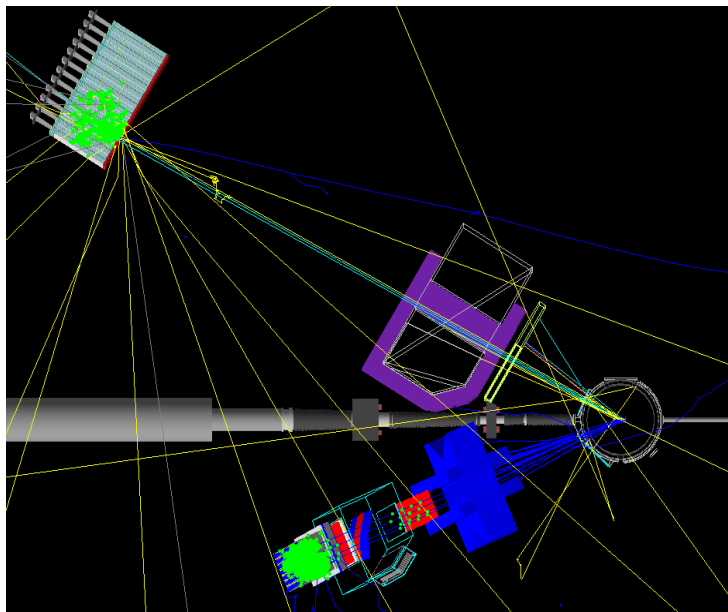


FIG. 9. Top view of the experimental apparatus model in G4SBS, shown in the high ϵ configuration. The beam direction is indicated, as well as the main elements (HCal, SBS magnet, BigBite spectrometer)

351 **A. Background and trigger rates**

352 The main processes expected to contribute to the trigger rates for the BigBite spectrom-
 353 eter are:

- 354 • the inelastic electron nucleon scattering process;

- 355 • photons from inclusive π^0 production;

- 356 • and to a lesser extent, charged pions.

357 Concerning HCal, various hadronic backgrounds are expected to contribute to the rates
 358 in HCal, the dominant ones being pions. Both the inelastic scattering and the inclusive
 359 neutral and charged pion production are implemented in G4SBS, the latter relying on the
 360 Wiser parametrization [28]. The minimum-bias “beam-on-target” generator (including all
 361 electromagnetic and hadronic processes) has also been considered for the HCal background.

362 The thresholds to apply to each arm are determined as a function of the elastic peak. For
 363 the electron arm, the threshold has been set at $\mu_E - 2.5\sigma_E$, μ_E and σ_E being respectively
 364 the position and width of the fitted elastic peak. Fig. 10 presents the distributions of rate
 365 of energy deposit for the different processes involved in the BigBite trigger rates.

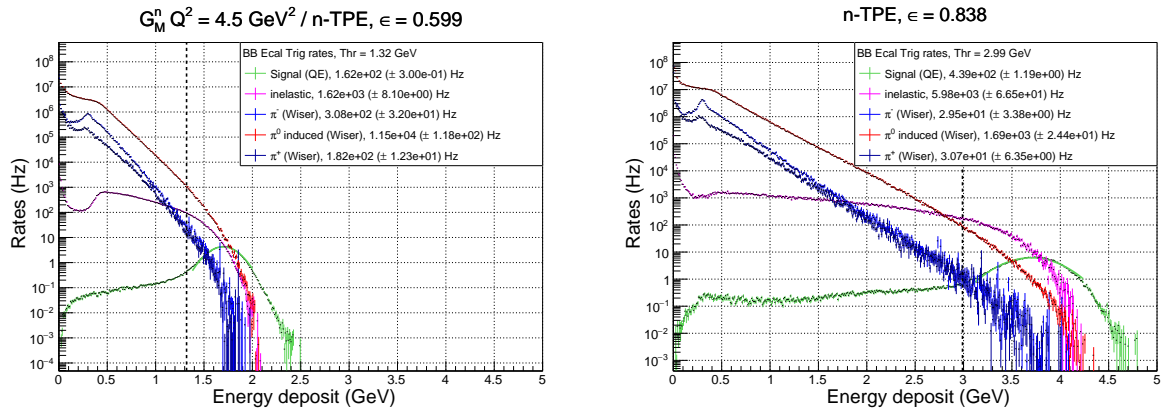


FIG. 10. Rates of the different process contributing to the BigBite electron arm trigger, for the low ϵ (left) and the high ϵ (right). Quasi-elastic is in green, inelastic in magenta, π^0 in red, π^- in blue, and π^+ in dark blue. Note the resolution for the elastic peak in the BigBite shower is ~ 0.3 GeV.

366 Since HCal is a sampling calorimeter (meaning that only a fraction of the shower energy
 367 is measured), its resolution is relatively wide (~ 0.7 GeV). Due to this, the threshold is at
 368 90% efficiency (which corresponds to ~ 0.1 GeV for both kinematics. Fig. 11 presents the
 369 distributions of rate of energy deposit for the different processes involved in the HCal trigger
 370 rates.

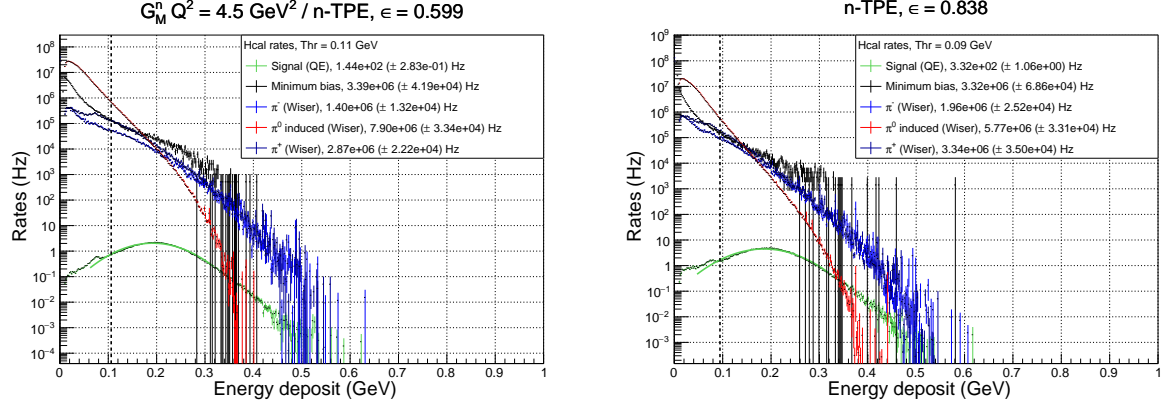


FIG. 11. Rates of the different process contributing to the HCal trigger, for the low ϵ (left) and the high ϵ (right). Quasi-elastic is in green, minimum bias in black, π^0 in red, π^- in blue, and π^+ in dark blue. Note the peak itself is around 0.2 GeV for 3.2 GeV nucleons.

372 The thresholds and trigger rates for each arm, as well as the coincidence rate (assuming
 373 30ns coincidence window), are summarized in Table. II. Note that for HCal, the “total rates”
 375 is either the “minimum bias” beam on target, *or* the sum of inclusive charged and neutral
 376 pions evaluated with the Wiser cross sections. Comparisons between Wiser and minimum
 377 bias at very low energy shows that the Wiser code results dramatically overestimate the
 378 HCal rates, henceforth the HCal rates estimations using minimum bias are deemed more
 379 reliable (and emphasized in Table. II). For the sake of thoroughness, we have checked the
 380 coincidence rates assuming the sum of the inclusive pions (evaluated with the Wiser cross
 381 sections) as the HCal rates.

382 *Assuming this worst case scenario*, the coincidence rates could be as high as 5kHz, which
 383 might be at the limit of manageability for the DAQ. However, even if those rates were proven
 384 to be accurate, a slight increase on the HCal threshold (which would drop the efficiency from
 385 $\sim 90\%$ to $\sim 85\%$) would decrease the total HCal rates by $\sim 35\%$ to 40% in this worst case
 386 scenario, which would make the situation more manageable (3.3 kHz). In the more reasonable
 387 case where the HCal rates are more accurately described by the minimum bias prediction,
 388 the coincidence will be lower than 2kHz, rate at which the SBS DAQ should operate safely.

Point (ϵ)	1 (0.599)		2 (0.838)	
	BigBite rates (Hz)	HCal rates (Hz)	BigBite rates (Hz)	HCal rates (Hz)
threshold (GeV)	1.32	0.106	2.99	0.090
Quasi-elastic	1.62×10^2	1.44×10^2	4.39×10^2	3.48×10^2
Inelastic	1.62×10^3	-	5.98×10^3	-
π^- (Wiser)	3.08×10^2	1.40×10^6	2.95×10^2	1.96×10^6
π^0 (Wiser)	1.15×10^4	7.90×10^6	1.69×10^3	5.77×10^6
π^+ (Wiser)	1.82×10^2	2.87×10^6	3.07×10^2	3.34×10^6
Minimum bias	-	3.39×10^6	-	3.32×10^6 (*)
Total	1.37×10^4	3.39×10^6	8.17×10^3	3.32×10^6
$(\sum_{\pi(Wiser)} \text{for HCal})$		/ (1.22×10^7)		/ (1.11×10^7)
Coincidence rate	1.39×10^3		8.14×10^2	
$(\sum_{\pi(Wiser)} \text{for HCal})$	(5.01×10^3)		(2.72×10^3)	

TABLE II. Trigger rates for BigBite and HCal, with the different process contributions separated, and the sum. For HCal, the total rates is either estimated with the minimum bias generator or the sum of inclusive pions estimated with the Wiser cross section. The coincidence rates assume a 30 ns coincidence window.

389 B. Contamination from inelastic

390 The main source of contamination for the quasi-elastic comes from the inelastic electron-
 391 nucleon scattering. Our quasi-elastic $e - N$ MC generator uses the Kelly form factor fits [].
 392 Our inelastic resonant $e - N$ MC generator uses the model by P. Bosted and E. Christy [].
 393 This model is a fit of $e - N$ data in the resonance region from Jefferson Lab Hall C [] which
 394 covers $0 \leq Q^2 < 8(\text{GeV}/c)^2$, with beam energies up to 5.5 GeV. According to [], the fit
 395 residue to the data between 4 and 6 GeV fluctuates by $\pm 10\%$. We assume a 20% systematic
 396 uncertainty on our inelastic cross section.

397 The relevant variables to select the quasi-elastic $e - N$ scattering from the resonant

³⁹⁸ $e - N$ scattering are the missing mass $W^2 = M_N^2 + 2M_N^2(E - E') - Q^2$, evaluated with
³⁹⁹ the BigBite resolution, of the system $N(e, e')X$, and the transverse missing momentum.
⁴⁰⁰ Figure 12 displays the event distributions in W^2 for both our simulated quasi-elastic and
⁴⁰¹ inelastic samples within the following set of fiducial acceptance cuts:

- ⁴⁰² • the electron track is reconstructed in BigBite;
- ⁴⁰³ • the total energy deposited in the BigBite calorimeter is above the 3 GeV threshold for
⁴⁰⁴ an average 4.2 GeV elastic peak (for $\epsilon = 0.84$ kinematic);
- ⁴⁰⁵ • the electron track must fire at least 3 PMTs in the GRINCH detectors;
- ⁴⁰⁶ • the total energy deposited in HCal is above the 0.10 GeV threshold. This corresponds
⁴⁰⁷ to 90% efficiency of the 3.2 GeV/c nucleons which deposit 0.20 GeV in the HCal
⁴⁰⁸ (scintillator material).

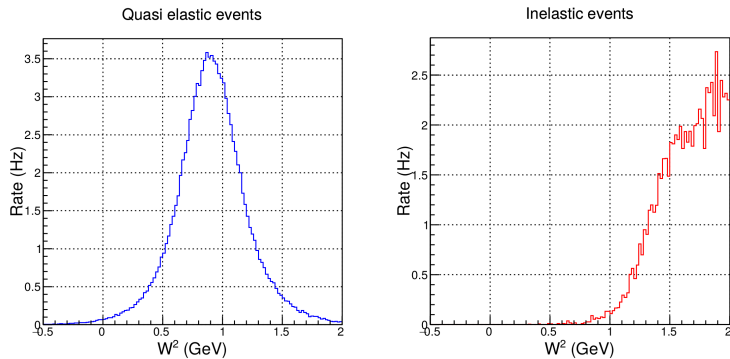


FIG. 12. Event distributions in $W^2 = M_N^2 + 2M_N^2(E - E') - Q^2$ for quasi elastic $e - N$ (left) and inelastic resonant $e - N$ (right) within the fiducial analysis cuts.

⁴⁰⁹ Before reconstructing the nucleon momentum, it is necessary to apply a selection cut on
⁴¹⁰ W^2 to reject a fraction of the inelastic events. To this end, only events for which $W^2 <$
⁴¹¹ 1.10 GeV 2 are selected for further discussion. Within this selection, our total number of
⁴¹² events counts 97% of quasi-elastic and 3% of inelastic.

⁴¹³ Now we will discuss the missing perpendicular momentum. The nucleon momentum and
⁴¹⁴ direction is reconstructed using the position of the HCal cluster, on the first step *under*

415 the assumption that it is a neutron. We use the direction of the virtual photon vector \vec{q}
 416 (corrected with the vertex position) to project the expected neutron position. The difference
 417 between the reconstructed and the projected nucleon position is shown, projected on x (the
 418 non-dispersive direction) and y (the dispersive direction), for both quasi-elastic and inelastic
 419 events on figure 13. We clearly distinguish in each case two structures, one which can be

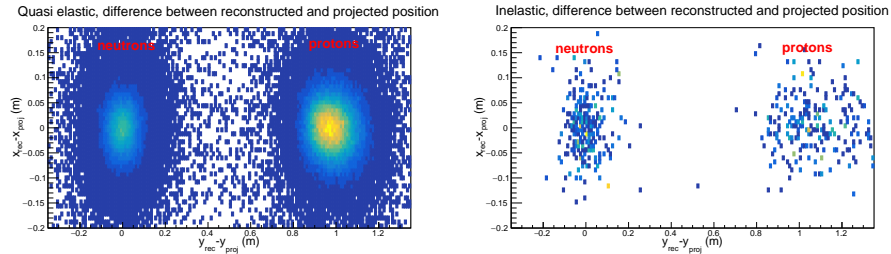


FIG. 13. Difference of projected position and reconstructed position for the nucleons in x (non-dispersive direction) and y (dispersive direction), for quasi-elastic events (left) and inelastic events (right). On each plot We clearly notice two structures. The structure on the left, centered at 0, is due to the neutrons. The structure on the right, shifted by about 1 m is due to the protons, which are deflected upwards by the magnetic field.

420
 421 identified a the neutrons, centered on zero in both x and y , and one which can be identified
 422 as the protons, which are deflected upwards and are shifted by about 1 m in y . Figure 14
 423 also shows the difference between the reconstructed and the projected nucleon position,
 424 except projected on y (the dispersive direction), for both the quasi-elastic and inelastic
 425 events. Comparing both the expected inelastic and elastic yields in this variable side-by-side
 426 evidences further the important role of the $W^2 < 1.10 \text{ GeV}^2$ selection to filter out inelastic
 427 events.
 428

430 As a second step, for the nucleons identified as protons (based on the location of the
 431 HCal cluster position with respect to its projected position), we need to correct the HCal
 432 reconstructed position y_{rec} by the average shift $\Delta y_{p,avg}$ observed in figure 13 for the nucleons
 433 identified as protons.

434 The nucleon momentum norm $p' = |\vec{p}'|$ is assumed to be equal to the virtual photon norm
 435 $|\vec{q}|$. With this information we can calculate the proton shift Δy_p for each proton.

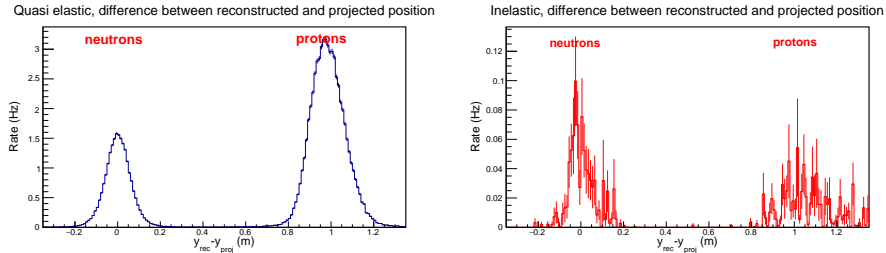


FIG. 14. Difference of projected position and reconstructed position for the nucleons projected in y (dispersive direction), compared between quasi-elastic (left) and inelastic (right) events. The selection for these distributions are the fiducial cuts $W^2 < 1.10 \text{ GeV}^2$. We may notice that the selection on $W^2 < 1.10 \text{ GeV}^2$ already reduces drastically the proportion of inelastic with respect to quasi elastic. We may also see that the distribution for the proton is slightly wider.

With this information we may build the transverse components of the nucleon momentum (in the SBS coordinates system) $p'_{x,SBS}$ and $p'_{y,SBS}$. For both the protons and neutrons, $p'_{x,SBS}$ can be written as $p'_{x,SBS} = p' \times (x_{rec} - v \sin \theta_{SBS}) / (D_{HCal} - v \cos \theta_{SBS})$ (with v the reconstructed vertex position, D_{HCal} the HCal distance to the target and θ_{SBS} the spectrometer angle. For the neutrons, $p'_{y,SBS}$ is $p'_{y,SBS} = p' \times y_{rec} / (D_{HCal} - v \cos \theta_{SBS})$. For the protons, $p'_{y,SBS}$ must be written as $p'_{y,SBS} = p' \times (y_{rec} - \Delta y_p) / (D_{HCal} - v \cos \theta_{SBS})$.

The nucleon momentum components in the SBS coordinates system $p'_{x,SBS}$ and $p'_{y,SBS}$ can then be transformed (using the corrected HCal distance to the target $D_{HCal} - v \cos \theta_{SBS}$) into the nucleon momentum components in the Hall A coordinate system p'_x , p'_y and p'_z , with the best resolution achievable.

In Hall A coordinate system, using the nucleon meomentum combined with the virtual photon vector \vec{q} , we may reconstruct the transverse missing momentum $p_{\perp miss} = \sqrt{(q_x - p'_x)^2 + (q_y - p'_y)^2}$, which is another very powerful variable to reject more inelastic background. Figure 15 displays the event distributions in $p_{\perp miss}$ for our simulated quasi-elastic sample within our fiducial acceptance cuts, and requiring $W^2 < 1.10 \text{ GeV}^2$. After selection on $W^2 < 1.10 \text{ GeV}^2$ and $p_{\perp miss} < 0.1 \text{ GeV}$, the inelastic contamination of our quasi-elastic sample is better than 1%, with 0.2% systematic uncertainties.

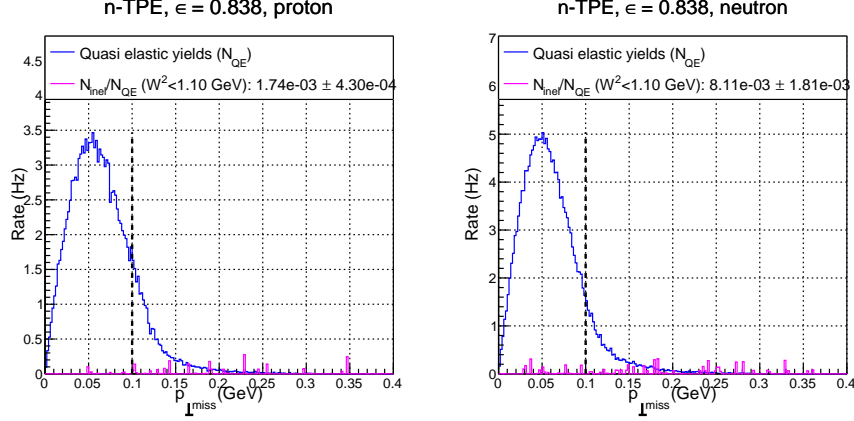


FIG. 15. Compared quasi-elastic (blue) and inelastic (magenta) distributions for $p_{\perp miss} = \sqrt{(q_x - p'_x)^2 + (q_y - p'_y)^2}$, within fiducial analysis cuts, after requiring $W^2 < 1.10 \text{ GeV}^2$, for the high ϵ kinematic, separated between protons on the left and neutrons on the right). The inelastic contamination of quasi-elastic events and their error bars are quoted in the legends.

454

C. Quasi-elastic counting rates

455 The signals for this experiment have been generated using the G4SBS elastic/quasi-elastic
 456 generator. We generated a reasonably large sample of quasi-elastic events N_{Gen} for each
 457 kinematics, within a solid angle $\Delta\Omega_{Gen}$ that was larger than the detector acceptance. To
 458 evaluate the detector solid angle, we define simple criteria that each event has to pass, defined
 459 as follows:

- 460 • require a primary track, going through all 5 GEM layers (electron arm);
 461 • require non-zero energy deposit in both the preshower and shower (electron arm);
 462 • require non-zero energy deposit in HCal (hadron arm).

463 The detector solid angle, for both proton and neutron, are defined in Table III. We also
 464 define there the p - n acceptance asymmetry $A_{\Delta\Omega}$ such as:

$$A_{\Delta\Omega} = \frac{(\Delta\Omega_e \otimes \Delta\Omega_n) - (\Delta\Omega_e \otimes \Delta\Omega_p)}{(\Delta\Omega_e \otimes \Delta\Omega_n) + (\Delta\Omega_e \otimes \Delta\Omega_p)} \quad (12)$$

Point (ϵ)	$\Delta\Omega_e$ (msr)	$\Delta\Omega_e \otimes \Delta\Omega_n$ (msr)	$\Delta\Omega_e \otimes \Delta\Omega_p$ (msr)	$A_{\Delta\Omega}$ (%)
1 (0.599)	52.4	46.7	47.2	0.5
2 (0.838)	32.7	20.8	22.2	3.0

TABLE III. Kinematics electron solid angle, and convoluted electron/hadron solid angle, and acceptance asymmetry.

Then, we evaluate the detection efficiency. For the electron, we require the energy reconstructed in the BigBite calorimeter to be above a threshold defined as $thr = \mu_E - 2.5 * \sigma_E$, as well as a minimum number of GRINCH PMTs fired due to the primary electron; For HCal, we select a threshold that yields 90% efficiency. These values are summarized in Table. IV.

Quasi-elastic selection efficiency η_{sel} are also provided.

Point (ϵ)	BB thr. (GeV)	HCal thr. (GeV)	$\eta_{det\ e}$	$\eta_{det\ n}$	$\eta_{det\ p}$	$\eta_{sel\ n}$	$\eta_{sel\ p}$
1 (0.599)	1.32	0.11	0.902	0.904	0.892	0.589	0.605
2 (0.838)	2.99	0.09	0.808	0.889	0.882	0.617	0.647

TABLE IV. Kinematics electron thresholds, particle detection efficiencies (η_{det}), and efficiency of quasi-elastic selection η_{sel} separated for the proton and the neutron.

The counting rates are evaluated using among the N_{Gen} events generated the events that have passed the selection described below, and weighting those events with the cross section $d\sigma/d\Omega|_i$ calculated by G4SBS, multiplied by the generation solid angle $\Delta\Omega_{Gen}$, using the formula:

$$N_{est} = \frac{\mathcal{L}_{exp}\Delta t}{N_{Gen}} \times \sum_{i \in \text{accepted evts}} \left(\frac{d\sigma}{d\Omega}|_i \times \Delta\Omega_{Gen} \right) , \quad (13)$$

where Δt the running time and \mathcal{L}_{exp} the experimental luminosity. \mathcal{L}_{exp} can be calculated as follows:

$$\mathcal{L}_{exp} = \frac{I_{exp}}{q_e} \cdot L_{tgt} \cdot d_{tgt} \frac{\mathcal{N}_A}{m_D} , \quad (14)$$

476 where I_{exp} is the beam current, q_e is the electron charge, L_{tgt} and d_{tgt} are the target length
 477 and density respectively, N_A is Avogadro's number, and m_D is the deuterium mass number.
 478 Events are “accepted” if they meet the following criteria:

- 479 • the electron is in the BigBite acceptance;
- 480 • the electron passes the BigBite threshold defined in Table IV and gives signal in the
 481 GRINCH;
- 482 • the nucleon is in the HCal acceptance and passes the HCal threshold defined in Ta-
 483 ble IV;
- 484 • the event passes the quasi-elastic selection defined in the previous section *i.e.* $W^2 \leq 1.1 \text{ GeV}^2$
 485 and $p_{\perp miss} \leq 0.10 \text{ GeV}$.

486 The total quasi-elastic statistics N_{QE} , as well as the total form factor, F^2 :

$$F^2 = \frac{N_{QE}}{\mathcal{L}_{exp} \cdot \Delta t \cdot d\sigma_{Mott}/d\Omega \cdot \Delta\Omega \cdot \eta} \quad (15)$$

487 and its statistical error $\Delta F^2 = F^2 / \sqrt{N_{QE}}$ are compiled for both kinematics in Table. VI,
 488 assuming a running time $\Delta t = 12$ hours of running at a beam intensity of $I_{exp} = 30 \mu\text{A}$ on
 489 a liquid deuterium target with length $l_{tgt} = 15 \text{ cm}$ and density $d_{tgt} = 0.169 \text{ g.cm}^{-3}$. In
 490 Eq. 13, $\Delta\Omega$ is the convoluted BigBite-HCal solid angle, and η is the product of all efficiencies
 491 (detection efficiencies $\eta_{det} \times$ selection efficiency η_{sel}).

Point (ϵ)	N_{QE} (e-n)	N_{QE} (e-p)	F_n^2 ($\times 10^{-3}$)	ΔF_n^2 ($\times 10^{-6}$)	F_p^2 ($\times 10^{-3}$)	ΔF_p^2 ($\times 10^{-6}$)
1 (0.599)	9.07×10^5	2.55×10^6	0.99	1.04	2.73	1.70
2 (0.838)	1.94×10^6	5.83×10^6	0.72	0.52	1.93	0.80

TABLE V. Quasi-elastic counting rates, and total form factor (defined in Eq. 11).

492 The calculation of the F_2 term requires the evaluation of the Mott cross section:

$$\sigma_{Mott} \equiv \frac{d\sigma_{Mott}}{d\Omega} = (\hbar c \alpha_{EM})^2 \frac{1}{4E^2} \left(\frac{\cos \theta_e/2}{\sin^2 \theta_e/2} \right)^2 \frac{E'}{E} \quad (16)$$

⁴⁹³ The Mott cross section has been calculated with the weighted average of the electron variables
⁴⁹⁴ (momentum and polar angle).

Point (ϵ)	$\langle \theta_e \rangle$ (deg)	$\langle k' \rangle$ (GeV)	$\langle Q^2 \rangle$ (GeV 2)	σ_{Mott} (nb sr $^{-1}$)
1 (0.599)	41.88	2.0	4.5	6.62
2 (0.838)	23.23	4.2	4.5	44.2

TABLE VI. The Mott cross section weighted average of kinematic variables over the BigBite acceptance.

495

VII. SYSTEMATIC ERRORS

496 In this section we will estimate (or set upper limits on) the contributions to the sys-
 497 tematic uncertainty for this experiment. The sources of systematic uncertainties from the
 498 experimental setup (target, acceptance, inelastic contamination) were already estimated for
 499 the SBS G_M^n experiment proposal [19]. Note that a majority of the potential sources of sys-
 500 tematic uncertainties (nuclear corrections, accidentals, radiative corrections, target density,
 501 etc) cancel in the ratio $R = f_{corr} \times N_{e,e'n}/N_{e,e'p}$, which is one of the strengths of this experi-
 502 mental method. The sources of uncertainties as well as their estimation for each kinematic
 503 is provided in Table. VII. Since the experimental setup has evolved since then, some of these
 504 uncertainties have been reevaluated, namely the acceptance loss and inelastic contamination.
 505 Table. IX lists the estimated contributions to systematic errors on the two-photon-exchange

TABLE VII. Estimated contributions (in percent) to the systematic error on $R = f_{corr} \times N_{e,e'n}/N_{e,e'p}$. Quantities marked with * are taken from the SBS G_M^n experiment proposal [19].

The total systematic errors on R is the quadratic sum of all other errors.

Kinematic (ϵ)	(1) 0.599	(2) 0.838
Acceptance losses	0.5 %	3.0 %
Inelastic contamination	0.9 %	0.6 %
Nucleon mis-identification*	0.6 %	
Syst. error on $R = f_{corr} \times N_{e,e'n}/N_{e,e'p}$ (Quadratic sum of the errors above)	1.3 %	3.1 %

506

508

509 contribution (TPE). The systematics for S^p and $\mu_n G_E^n/G_M^n$ have already been explicated in
 510 Sec. III, and are the leading contributions to the total uncertainty.

511 Inelastic contamination has been reevaluated in Sec. VI B. To evaluate the upper limit on
 512 our uncertainty, we added quadratically the inelastic contamination evaluated for the proton
 513 and the neutron for each kinematics. This would be the error that we make on R if we ignore

TABLE VIII. Estimated contributions to systematic error on the Rosenbluth slope.

Syst. error on p cross section ($S^p = \sigma_L^p / \sigma_T^p$)	0.01
Syst. error on n form factor ($\mu_n G_E^n / G_M^n$)	0.05
Syst. error on Rosenbluth slope (TPE)	0.012

the inelastic contamination in the quasi-elastic $e - n$ and $e - p$ samples. Even in this case, we expect less than 1% systematic errors. Of course, we do plan to reevaluate and subtract the inelastic contamination from our actual data sample, so the quoted systematic uncertainty coming from inelastic contamination should be a upper limit.

The acceptance loss in SBS (*i.e.* the proportion of non-detected nucleons for each detected electron) have been evaluated for both kinematics. They are about 10% for the $\epsilon = 0.60$ kinematic (meaning that for every good electron measured, we will not measure the recoil nucleon 10% of the times), but they are over 30 % for the $\epsilon = 0.84$ kinematics, which is due to a larger spread of the nucleon imprint. The systematic uncertainty on the acceptance loss for the ratio $R = f_{corr} \times N_{e,e'n} / N_{e,e'p}$ is maximized by the proton-neutron solid angle asymmetry $A_{\Delta\Omega} = \Delta\Omega_n - \Delta\Omega_p / \Delta\Omega_n + \Delta\Omega_p$. This asymmetry is about 0.5% for the $\epsilon = 0.60$ kinematic (consistent with the G_M^n proposal), but goes up to 3% for the $\epsilon = 0.84$ kinematics.

526

VIII. BEAM TIME REQUEST

527 We request 48 hours total time (32 PAC hours of beam-on target) to measure
 528 the two-photon effect (and G_E^n in one-photon approximation) at $Q^2 = 4.5$ (GeV/c)² through
 529 a measurement of the cross sections of the reaction D(e,e'N) at a large value of the virtual
 530 photon polarization $\epsilon=0.84$. *The measurement at $Q^2 = 4.5$ (GeV/c)², $\epsilon=0.60$ is already*
 531 *scheduled as part of the SBS G_M^n experiment E12-09-019 [19].*

532 We plan to take 12 hours of data at a full luminosity of $2.86 \times 10^{38} \text{ cm}^{-2}\text{s}^{-1}$, which
 533 corresponds to a beam intensity of $I_{exp} = 30 \mu\text{A}$ on a liquid deuterium target with length
 534 $l_{tgt} = 15 \text{ cm}$ and density $d_{tgt} = 0.169 \text{ g.cm}^{-3}$. To have a better handle on our backgrounds,
 535 we also plan to take 12 hours of data at half luminosity (basically by lowering the beam
 536 intensity by a factor 2). In each of these configurations, we also need to take data on a
 537 “dummy” target (*i.e.* on a target cell identical to the one used for production, but empty)
 538 to understand the contamination of our data from the target walls.

539 In addition to this beam time, we also require 16 hours (two shifts) to change the exper-
 540 imental configuration. This configuration change means:

- 541 • BigBite spectrometer angle and distance change;
 - 542 • Beam pass change (from 4.4 GeV/2 pass to 6.6 GeV/3 pass);
- 543 If this experiment is approved, we plan to insert this experiment in the GMn E12-09-019
 544 run plan in such a way that we can avoid a change in configuration for the SBS magnet
 545 and the HCal, which is very time consuming. Table. IX displays an excerpt of the GMn run
 546 plan, and points out where the nTPE measurement inserts. The beam pass change and the
 547 BigBite move may be done in parallel, and should take one shift (eight hours). We require
 548 an additional shift (eight hours) for beam tuning after beam pass change. The projected use
 549 of this time is summarized in Table. XI.

552 This experiment will take place in Hall A, along the already scheduled SBS G_M^n experiment
 553 E12-09-019, utilizing the BigBite spectrometer to detect electrons scattered off the liquid
 554 deuterium target, and HCal calorimeter to detect the recoiling neutron and proton.

TABLE IX. Excerpt of GMn E12-09-019 run plan table, showing where the $\epsilon = 0.84$ measurement would be inserted in our run plan. The $\epsilon = 0.60$ measurement is also emphasized in blue.

Step #	task	Q^2 (GeV/c) ²	$\theta_{BB} / \theta_{SBS}$ degrees	Beam GeV	Time hours	Tech work time (h)
4b (install GEn-RP)	GEn-RP		41.9 / 24.7	-	4	4
4c (GEn-RP)	Production	4.5	41.9 / 24.7	4.4	104 (calendar) (52 PAC hours)	
4d (remove GEn-RP)	GEn-RP		41.9 / 24.7	-	56	24
4e (GMn/nTPE low ϵ)	Production	4.5	41.9 / 24.7	4.4	64 (calendar) (32 PAC hours)	
5a (conf. change)	BB/SBS/HCal		32.5 / 31.1	-	32	16
5b (beam tune)	beam		32.5 / 31.1	4.4	4	
5c (GMn)	Production	3.5	32.5 / 31.1	4.4	64 (calender) (32 PAC hours)	
6a (pass change)	beam/BB		23.2 / 31.1	6.6	8	4
6b (beam tune)	beam		23.2 / 31.1	6.6	8	
6c see Table. X	Production	4.5	23.2 / 31.1	6.6	64 (calendar) (32 PAC hours)	
7a (conf. change)	BB/SBS/HCal		58.4 / 17.5		32	16
+ (pass change)	beam		58.4 / 17.5	4.4	during SBS move	
7b (beam tune)	beam	-	58.4 / 17.5	4.4	4	
7c	Production	5.7	58.4 / 17.5	4.4	50 (calendar) (25 PAC hours)	

555 Data taking (if approved by PAC48) will take place in summer 2021 during the approved
 556 and scheduled run of the GMn, E12-09-019, experiment, which is going to measure the $e - n$
 557 elastic scattering cross section at $Q^2 = 4.5$ (GeV/c)² at $\epsilon=0.60$.

558 The set of instrumentation and required beam current for proposed measurement is iden-

TABLE X. Summary table for the beam time request. Setting changes include SBS and BigBite angles change, as well as a beam pass change from 4.4 GeV (2 pass) to 6.6 GeV (3 pass). This beam pass change can mostly be done in parallel to the SBS

Task	Target	I_{exp}	time requested
Data taking (Prod.)	15 cm LD ₂	30 μ A	12 hours
Data taking (Syst.)	15 cm “Dummy”	30 μ A	4 hours
Data taking (Prod.)	15 cm LD ₂	15 μ A	12 hours
Data taking (Syst.)	15 cm “Dummy”	15 μ A	4 hours
Setting changes (BigBite move, beam pass change)			8 hours
Beam tune after beam pass change			8 hours
Total			48 hours

559 tical to one in the GMn experiment. The beam energy of 6.6 GeV will be used. One of two
 560 data points required for the cross section LT separation is already in the data taking plan of
 561 GMn.

562 There are no other measurements of TPE in the $e - n$ elastic scattering and knowledge
 563 of the TPE is essential for the understanding of the elastic electron scattering from neutron
 564 (and proton) and hadron structure. Furthermore, it is a necessary input in the analysis and
 565 interpretation of a wide range of electron scattering processes.

566 The kinematics of our measurements emphasize the same Q^2 range where TPE in $e - p$
 567 elastic scattering was observed to dominate in Rosenbluth slope. Measuring at this high
 568 momentum transfers will provide unique input for testing TPE calculations [4].

569 We propose to measure the Rosenbluth slope and extract (in one-photon approximation)
 570 $\delta G_E^n/G_M^n$ to an accuracy of 0.15, which would bring its precision to a level comparable with
 571 that of the double polarization experiments GEN-RP and GEN-He3 at such value of Q^2 .
 572 Such precision should be sufficient to detect the TPE contribution to the $e - n$ Rosenbluth
 573 slope on the three sigma level.

-
- 574 [1] R. Hofstadter, *Rev. Mod. Phys.* **28**, 214 (1956).
- 575 [2] M. N. Rosenbluth, *Phys. Rev.* **79**, 615 (1950).
- 576 [3] E. Christy *et al.*, “Two-photon exchange in electron-proton elastic scattering at large four-momentum transfer,” (2020), in preparation for publication in PRL.
- 577
- 578 [4] P. G. Blunden, W. Melnitchouk, and J. A. Tjon, *Phys. Rev.* **C72**, 034612 (2005), arXiv:nucl-th/0506039 [nucl-th].
- 579
- 580 [5] J. Arrington, P. G. Blunden, and W. Melnitchouk, *Prog. Part. Nucl. Phys.* **66**, 782 (2011), arXiv:1105.0951 [nucl-th].
- 581
- 582 [6] A. Afanasev, P. Blunden, D. Hasell, and B. Raue, *Prog. Part. Nucl. Phys.* **95**, 245 (2017), arXiv:1703.03874 [nucl-ex].
- 583
- 584 [7] B. Wojtsekhowski, in *Exclusive processes at high momentum transfer. Proceedings, Newport News, USA, May 15-18, 2002* (2002) arXiv:1706.02747 [physics.ins-det].
- 585
- 586 [8] G. D. Cates, C. W. de Jager, S. Riordan, and B. Wojtsekhowski, *Phys. Rev. Lett.* **106**, 252003 (2011), arXiv:1103.1808 [nucl-ex].
- 587
- 588 [9] C. D. Roberts, M. S. Bhagwat, A. Holl, and S. V. Wright, *Eur. Phys. J. ST* **140**, 53 (2007), arXiv:0802.0217 [nucl-th].
- 589
- 590 [10] J. Segovia, I. C. Cloet, C. D. Roberts, and S. M. Schmidt, *Few Body Syst.* **55**, 1185 (2014), arXiv:1408.2919 [nucl-th].
- 591
- 592 [11] B. Wojtsekhowski (2020) arXiv:2001.02190 [nucl-ex].
- 593
- 594 [12] G. A. Miller, *Phys. Rev. Lett.* **99**, 112001 (2007), arXiv:0705.2409 [nucl-th].
- 595
- 596 [13] C. E. Carlson and M. Vanderhaeghen, *Phys. Rev. Lett.* **100**, 032004 (2008), arXiv:0710.0835 [hep-ph].
- 597
- 598 [14] D. Muller, D. Robaschik, B. Geyer, F. M. Dittes, and J. Horejsi, *Fortsch. Phys.* **42**, 101 (1994), arXiv:hep-ph/9812448 [hep-ph].
- 599
- 598 [15] X.-D. Ji, *Phys. Rev. Lett.* **78**, 610 (1997), arXiv:hep-ph/9603249 [hep-ph].
- 599
- 599 [16] A. V. Radyushkin, *Phys. Lett.* **B380**, 417 (1996), arXiv:hep-ph/9604317 [hep-ph].

- 600 [17] M. Diehl and P. Kroll, *Eur. Phys. J.* **C73**, 2397 (2013), arXiv:1302.4604 [hep-ph].
- 601 [18] N. Kivel, (2020), private communications.
- 602 [19] J. Annand, R. Gilman, B. Quinn, B. Wojtsekhowski, *et al.*, unpublished. See https://www.jlab.org/exp_prog/proposals/09/PR12-09-019.pdf, https://www.jlab.org/exp_prog/proposals/proposal_updates/PR12-09-019_pac35.pdf (2008).
- 603 [20] E. B. Hughes, T. A. Griffy, M. R. Yearian, and R. Hofstadter, *Phys. Rev.* **139**, B458 (1965).
- 604 [21] R. G. Arnold *et al.*, *Phys. Rev. Lett.* **61**, 806 (1988).
- 605 [22] L. Durand, *Phys. Rev.* **115**, 1020 (1959).
- 606 [23] E. E. W. Bruins *et al.*, *Phys. Rev. Lett.* **75**, 21 (1995).
- 607 [24] G. Kubon *et al.*, *Phys. Lett.* **B524**, 26 (2002), arXiv:nucl-ex/0107016 [nucl-ex].
- 608 [25] J. Lachniet *et al.* (CLAS), *Phys. Rev. Lett.* **102**, 192001 (2009), arXiv:0811.1716 [nucl-ex].
- 609 [26] V. Punjabi, C. F. Perdrisat, M. K. Jones, E. J. Brash, and C. E. Carlson, *Eur. Phys. J.* **A51**, 79 (2015), arXiv:1503.01452 [nucl-ex].
- 610 [27] A. Puckett, unpublished. See https://hallaweb.jlab.org/wiki/index.php/Documentation_of_g4sbs (2016).
- 611 [28] D. E. Wiser, “Photoproduction of protons, kaons and pions at slac energies,” Ph.D. thesis,
- 612 University of Wisconsin (1977).